Synthesis of novel hybrid decavanadate material (NH4)2(H2en)2V10O28.4H2O: Characterization, anticorrosion and biological activities

M. Idboumlik, M. Kadiri, N. Hamdi, M. Driouch, A.F.I. Ngopoh, I. Lakkab, E-E. Bendeif, M. Sfaira, B. El Bali, M. Lachkar, et al.

To cite this version:

M. Idboumlik, M. Kadiri, N. Hamdi, M. Driouch, A.F.I. Ngopoh, et al.. Synthesis of novel hybrid decavanadate material (NH4)2(H2en)2V10O28.4H2O: Characterization, anticorrosion and biological activities. Materials Chemistry and Physics, 2022, 287, pp.126211. ⟨10.1016/j.matchemphys.2022.126211⟩. ⟨hal-04393343⟩

HAL Id: hal-04393343
https://hal.science/hal-04393343v1

Submitted on 14 Jan 2024

Synthesis of novel hybrid decavanadate material $(NH_4)_2(H_2en)_2\{V_{10}O_{28}\}.4H_2O$: Characterization, anticorrosion and biological activities

M. Idboumlik[1], M. Kadiri[2], N. Hamdi[1], M. Driouch[2], A.F.I. Ngopoh[3], I. Lakkab[1], E-E. Bendeif[4], M. Sfaira[2], B. El Bali[5], M. Lachkar[1], and A. Zarrouk[6,*]

[1]*Engineering Laboratory of Organometallic, Molecular Materials and Environment (LIMOME), Faculty of Sciences, Sidi Mohamed Ben Abdellah University, Po. Box 1796 (Atlas), 30000 Fez, Morocco.*
[2]*Laboratory of Engineering, Modeling and Systems Analysis (LIMAS), Faculty of Sciences, Sidi Mohamed Ben Abdellah University, Po. Box 1796 (Atlas) 30000, Fez, Morocco.*
[3]*Université Marien Ngouabi, Faculté des Sciences et Techniques, BP 69, Brazzaville, République du Congo.*
[4]*CRM2, UMR CNRS 7036, Université de Lorraine, F-54506 Vandoeuvre-lès-Nancy, France.*
[5]*Independent Scientist, Oujda, Morocco; ORCID (https://orcid.org/0000-0001-6926-6286).*
[6]*Laboratory of Materials, Nanotechnology and Environment, Faculty of Sciences, Mohammed V University in Rabat, Av. Ibn Battuta. P.O. Box 1014, Rabat, Morocco.*

Corresponding author
Prof. Dr. Abdelkader Zarrouk
Email: azarrouk@gmail.com (AZ)
Phone: 00212665201397
Scopus Author ID: 36125763200
https://orcid.org/0000-0002-5495-2125

Abstract

Using ethylenediamine (en) as a structure-directing agent, a novel hybrid decavanadate $(NH_4)_2(H_2en)_2\{V_{10}O_{28}\}.4H_2O$ has been synthesized via a slow evaporation approach. A low-temperature single crystal X-ray diffraction investigation was used to investigate its structural structure. Its crystal structure was studied using a low temperature single crystal X-ray diffraction analysis. The asymmetric unit is made up of a single $[V_{10}O_{28}]^{6-}$ monomer, one $(NH_4)^+$, one ethylenediammonium $(H_2en)^{2+}$ cation and two H_2O molecules. Supramolecular interactions such as N─H···O and O─H···O hydrogen bonds build the three-dimensional network, ensuring connection between organic cations, water molecules, and the inorganic framework. The Fourier Transform Infrared result shows distinct bands associated to decavanadate moieties and organic molecules. The organic moieties, water molecules, and ammonium ions are all lost during the hybrid compound's thermal decomposition. The study of the corrosion inhibiting behavior of the decavanadate solution clearly showed a much stronger effect in acidic media than in neutral environment. However, the biological activity of $(NH_4)_2(H_2en)_2\{V_{10}O_{28}\}.4H_2O$ revealed humble results.

Keywords: Decavanadate hybrid material; Structural analysis; Corrosion inhibition; Biological activity.

1. Introduction

Making up to 150 ppm of the Earth's core, and comprises 0.014% of the Earth's crust, vanadium (V) is an extensively dispersed element generally occurring at low concentrations in about 65 minerals; almost 15×10^{-3} g is detected in a 75 Kg heavy human body [1,2]. Vanadium has three stable oxidation states: V^{+3}, V^{+4}, and V^{+5}, which have crucial biological significance, especially vanadates containing V^{+5}. The oxidation states -1 and +2 are unstable forms. V, as Mo and W, are oxidized to give polyoxometalates (POMs), which are anionic clusters based on oxo-complexes of transition metals; they have attracted considerable attention by virtue of having a variety of domains including catalysis, biology, materials science [3]. The polyoxovanadates (POVs) exhibit a large variety of structural features, ranging from metavanadates chains $[VO_3^-]_n$, oxides layered $[V_4O_{10}]$, to polyanions in a compact state $[V_{10}O_{28}]^{6-}$, depending on the synthesis conditions, especially medium concentration and pH [4]. Interestingly, Aureliano et al. reported on the decrease of the V^{+5}-coordination upon pH increases of the solutions aiming the crystals synthesis [5]. Indeed, for pH ≈ 6, one get a yellow solution containing essentially decavanadate core $(H_nV_{10}O_{28})^{n-6}$ (n = 0-4). For pH ≈ 6, a yellow solution containing essentially decavanadate core $(H_nV_{10}O_{28})^{n-6}$ (n = 0-4) is gotten. Increasing pH and changing concentration conditions produce other polyoxovanadates, with $[V_2O_7^{2-}]$ and $[V_4O_{12}^{4-}]$; whereas a decrease in ph eventually leads to the creation of additional decavanadate forms: $[HV_{10}O_{28}]^{5-}$, $[H_2V_{10}O_{28}]^{4-}$, $[H_3V_{10}O_{28}]^{3-}$, $[H_4V_{10}O_{28}]^{2-}$ [6]. The growing interest of these polyanions is due to their important biological activities such as interactions with lipid interfaces, insulin enhancing, cell death and probing muscle contraction [7].

Recently, V-based compounds have been investigated for corrosion inhibition of Al alloys as a suitable alternative to Chrome [8,9]. However, due to the relatively high solubility of vanadium oxides in aqueous solutions, the area has received little study[10,11]. In an investigation of the release kinetics and protection effectiveness of vanadate-based pigments in epoxy-coated

AA2014-T6 panels, Smith *et al.* [12] found that vanadates are effective pigments for safeguarding Al alloys. A later investigation by Iannuzzi *et al.* concluded that in aqueous solutions, at neutral to basic pH range, vanadates gave the best performance as inhibitor for Aluminum [13]. Based on these findings, we tested our new hybrid vanadate $(NH_4)_2(H_2en)_2\{V_{10}O_{28}\}.4H_2O$ as corrosion inhibitor for mild steel in both acidic medium 1 M HCl and neutral solution of 3% NaCl. Our choice aims to select the appropriate medium, and to study further the mechanism of corrosion inhibition by potentiodynamic polarization (PP) and electrochemical impedance spectroscopy (EIS) measurements. We hereby report on the synthesis, via a soft chemistry route, of the title compound. We discussed its spectroscopic and thermal features correlated to its crystal structure. Moreover, we reported on its corrosion inhibition, bactericidal inhibition and antioxidant activities.

2. Experimental, Materials and Methods

2.1. Synthesis and crystallization of $(NH_4)_2(H_2en)_2\{V_{10}O_{28}\}.4H_2O$

All of the reagents and solvents used for the reported researches were purchased from Sigma-Aldrich and employed without additional purification. Ammonium metavanadate $(NH_4)VO_3$ (300 mg, 2.5 mmol) diluted in 20 mL distilled water and kept at 90 °C with continuous agitation. The obtained light-yellow solution was allowed to cool to 50 °C and 80 mg (0.4 mmol) of $CuCl_2.4H_2O$ and 30 mg (0.5 mmol) of ethylenediamine were added before adjusting the brown color solution to pH 5 by adding HNO_3 acid. The mixture was further stirred about 30 min before to be filtered and kept at room temperature. Orange crystals rose after two weeks, which are suitable for X-Rays single crystal analysis. They have been washed with an ethanol-water (80-20%) mixture and dried at ambient conditions.

2.2. Single crystal X-ray diffraction measurements and structural determination

The single crystal X-ray diffraction measurements were acquired at 100 (2) K on a Bruker D8 Venture diffractometer, supplied with a two-dimensional CMOS detector (Bruker

PHOTON100), using the $Mo_{K\alpha}$-radiation (λ= 0.71073 Å). For the unit cell determination, the Bruker APEX package software [14] was employed, along with data reduction and analytical absorption adjustments. Direct techniques and consecutive Fourier difference syntheses were used to solve the appropriate structure in the space group P-1, and it was refined against F2 using weighted full-matrix least-squares methods in the SHELXL97 software [15]. The non-H atoms were polished in an anisotropic manner. The WinGX software package [16] was used to do all computations. The structural graphics were drawn using DIAMOND program [17]. Table 1 illustrates the crystal data, data gathering, and structural refinement information. The atomic coordinates are reported in Table 2. Table 3 and Table 4 show selected bond lengths and angles, as well as specifics of hydrogen bonding geometries. The CIF data file of the investigated compound may be found in the Cambridge Structural database under the number: **CCDC 2104907**. Copies of the published material can be acquired, free of charge, on application to the Director, CCDC, 12 Union Road, Cambridge CB2 1EZ, UK, fax: +44 (0)1223 336033 or Email: deposit@ccdc.cam.ac.uk

Table 1

Structure refinement, data collection, and crystal data of $(NH_4)_2(H_2en)_2\{V_{10}O_{28}\}.4H_2O$.

Chemical formula	$CH_9N_{1.50}O_8V_{2.50}$
M_r	297.45
Crystal system, space group	Triclinic, P\-1
Temperature (K)	100
a, b, c (Å)	8.4975(2), 10.2550(3), 10.9165(3)
α, β, γ (°)	103.950(2), 98.466(2), 113.978(3)
V (Å^3), Z	810.67(4), 4
F(000)	588
Radiation type / λ(Å)	Mo $K\alpha$ / 0.71073
Crystal sizes	?
μ (mm^{-1})	2.87
$R_{(int)}$	0.033
No. measured reflections	40050
No. independent reflections	8433
reflections with $I \geq 2\ \sigma(I)$	7918
θ_{max}, θ_{min}	37.9°, 2.0°
Reciprocal space	h = -14→14 k = -17→17 l = -18→18
$R[F^2 > 2\sigma(F^2)]/ wR(F^2)/S$	0.023/0.066/1.13

Table 2

Isotropic or equivalent isotropic displacement parameters and fractional atomic coordinates (Å^2) for $(NH_4)_2(H_2en)_2\{V_{10}O_{28}\}.4H_2O$.

	x	y	z	U(eq)
V(4)	6591	81531	74111	61
V(2)	18141	49001	47561	41
V(5)	11981	53491	75541	51
V1	40301	79811	69381	71
V(3)	12241	77031	46231	61
O(8)	13641	59211	35551	61
O1	13531	39201	60261	61
O(12)	5831	67871	83131	71
O(9)	12001	85751	35731	101
O(14)	35601	66541	79181	71
O(2)	39701	62091	55341	71
O(7)	18801	35011	36081	71
O(3)	35471	85801	55041	81
O(13)	11901	44991	86231	101
O(4)	31261	90681	79041	71
O(6)	10331	63231	59491	51
O(5)	61681	89861	75171	111
O(10)	5951	87261	59361	71
O(11)	1731	92721	84121	101
N(3)	6771	82431	108551	81
N(2)	34321	57831	18061	111
N1	70581	82321	48811	111
C1	59191	79461	35841	111
C(2)	52151	63051	27191	111
O(1W)	29781	28171	8171	151
O(2W)	41041	80731	6851	131

Equivalent atoms are generated via symmetry transformations: #1 -x,-y+1,-z+1.

Table 3

Selected bond lengths (Å) for complex $(H_2en)_2(NH_4)_2\{V_{10}O_{28}\}.4H_2O$.

V(4)-O(11)	1.6109(7)	V(5)-O(6)	2.2302(7)
V(4)-O(4)	1.8413(7)	V(5)-V(3)#1	3.0684(2)
V(4)-O(10)	1.8427(7)	V(5)-V1	3.0986(2)
V(4)-O(12)	1.8837(7)	V1-O(5)	1.6086(7)
V(4)-O(7)#1	2.0444(7)	V1-O(4)	1.8202(7)
V(4)-O(6)	2.3155(7)	V1-O(3)	1.8643(7)
V(4)-V1	3.0508(2)	V1-O(14)	1.8819(7)
V(4)-V(2)#1	3.0712(2)	V1-O(2)	2.0524(7)
V(4)-V(3)	3.1048(2)	V1-O(6)	2.3082(7)
V(2)-O(7)	1.6881(7)	V1-V(3)	3.0790(2)
V(2)-O(2)	1.6948(7)	V(3)-O(9)	1.6170(7)
V(2)-O1	1.8962(7)	V(3)-O(3)	1.7925(7)
V(2)-O(8)	1.9500(7)	V(3)-O(10)	1.8433(7)
V(2)-O(6)	2.0952(7)	V(3)-O(8)	1.9756(7)

V(2)-O(6)#1	2.1310(7)	V(3)-O1#1	2.0197(7)
V(2)-V1	3.0686(3)	V(3)-O(6)	2.2347(6)
V(2)-V(4)#1	3.0712(2)	V(3)-V(5)#1	3.0684(2)
V(5)-O(13)	1.6155(7)	O(8)-V(5)#1	2.0153(7)
V(5)-O(12)	1.8170(7)	O1-V(3)#1	2.0198(7)
V(5)-O(14)	1.8171(7)	O(7)-V(4)#1	2.0444(7)
V(5)-O1	1.9972(7)	O(6)-V(2)#1	2.1309(7)

To generate equivalent atoms, symmetry transformations are employed: #1 -x,-y+1,-z+1.

Table 4

Hydrogen bonding network in the framework of complex $(H_2en)_2(NH_4)_2\{V_{10}O_{28}\}.4H_2O$.

D-H...A	d(D-H)	d(H...A)	d(D...A)
C1-H1...O(10)#2	0.99	2.59	3.3412(12)
C1-H(2)...O(3)	0.99	2.46	3.2445(13)
N(3)-H(1N3)...O(11)#3	0.827(13)	2.143(14)	2.8882(11)
N(3)-H(1N3)...O(1W)#1	0.827(13)	2.541(17)	2.9649(12)
N(3)-H(2N3)...O(9)#4	0.819(13)	2.450(17)	2.8489(11)
N(3)-H(2N3)...O(13)#5	0.819(13)	2.066(13)	2.8564(11)
N(3)-H(3N3)...O(12)	0.813(12)	1.978(13)	2.7887(10)
N(3)-H(4N3)...O(5)#6	0.808(13)	2.144(14)	2.8970(11)
N(3)-H(4N3)...O(2W)#4	0.808(13)	2.597(18)	3.0167(12)
N(2)-H(1N2)...O(2W)	0.90(2)	1.93(2)	2.8009(12)
N(2)-H(2N2)...O(1W)	0.95(2)	1.95(2)	2.8110(13)
N(2)-H(3N2)...O(8)	0.87(2)	1.95(2)	2.7951(11)
N1-H(1N1)...O(2)	0.90(2)	2.12(2)	2.9217(11)
N1-H(1N1)...O(7)#7	0.90(2)	2.47(2)	2.9955(11)
N1-H(1N1)...O(5)	0.90(2)	2.613(19)	3.0812(12)
N1-H(2N1)...O(9)#2	0.86(2)	2.06(2)	2.9020(12)
N1-H(3N1)...O1#7	0.86(2)	2.39(2)	3.0720(11)
N1-H(3N1)...O(10)#8	0.86(2)	2.11(2)	2.8423(11)
O(1W)-H(1W1)...O(14)#7	0.928(10)	1.918(11)	2.8289(11)
O(2W)-H(1W2)...O(4)#2	0.939(10)	1.867(12)	2.7667(11)
O(2W)-H(2W2)...O(14)#9	0.935(9)	2.008(13)	2.8945(11)
O(1W)-H(2W1)...O(5)#7	0.937(9)	2.54(2)	3.0946(12)
O(1W)-H(2W1)...O(11)#1	0.937(9)	2.195(14)	3.0556(11)

Equivalent atoms are generated via symmetry transformations:
#1 -x,-y+1,-z+1 #2 -x+1,-y+2,-z+1 #3 -x,-y+2,-z+2
#4 x,y,z+1 #5 -x,-y+1,-z+2 #6 -x+1,-y+2,-z+2
#7 -x+1,-y+1,-z+1 #8 x+1,y,z #9 x,y,z-1

2.3. Infrared spectroscopy measurements

At room temperature, the FT-IR spectra of a powder formed of grounded crystals of the title compound was measured on a VERTEX 70 FTIR Spectrophotometer with a resolution of 4 cm^{-1} in the range 4000-400 cm^{-1}. The sample was analyzed in powder form (ATR technique).

2.4. Thermal analysis measurements

The thermogravimetric analysis was used to investigate the compond's thermal stability (TGA) measurements were performed as in the previous case. TGA data were collected using an SDT-Q600 analyzer from TA instruments. The sample is heated from room temperature to 600 °C at a rate of 10 °C min^{-1}. Samples were measured in open platinum crucibles with air flow.

2.5. Electrochemical measurements

Solutions for electrochemical tests were prepared by dissolving the new hybrid compound of decavanadate $(NH_4)_2(H_2en)_2(V_{10}O_{28}).4H_2O$ as corrosion inhibitor in two electrolytic media. The hydrochloric acid solution was obtained by dilution of concentrated acid (37%, d= 1.19). The second electrolyte was 3% of NaCl, which had a purity ≥ 99% by dissolution in distillated water. The working mild steel (MS) electrode was rectangular with the following chemical composition 0.370% C, 0.230% Si, 0.680% Mn, 0.016% S, 0.077% Cr, 0.011% Ti, 0.059% Ni, 0.009% Co, 0.160% Cu and the remainder iron (Fe). The working electrode was coated by a resin to delimitate the surface area exposed to the electrolyte solution of 1 cm^2, and was abraded using 120 to 2000 grit emery papers, rinsed with distilled water, degreased in acetone, and freshly washed with bi-distilled water.

The electrochemical experiments were performed in the conventional three-electrode cell using a platinum counter electrode (CE) and Ag/AgCl 3M KCl as reference electrode. All these experiments were conducted by the BioLogic SP-150 device, controlled with analysis software (Ec-Lab® V11.20). For potentiodynamic polarization (PP) measurements, the potential was scanned at a sweep rate of 1 mV s^{-1} in bearing potential range of -250 mV to +250 mV versus the open circuit potential. Electrochemical impedance spectroscopy (EIS) measurements were performed at corrosion potential in the frequency range of 100 kHz to 100 mHz and an AC voltage amplitude of 10 mV peak to peak. The working electrode was immersed in the test solution for 30 minutes prior to the PP and EIS measurements to establish a steady state potential. All experiments were repeated, minimum in triplicate, and the temperature of cell was controlled by a thermostatic water bath.

2.6. UV-visible

The electronic spectrum was carried out by using a Camspec, M 550 Double Beam scanning UV-visible spectrophotometer using a quartz cell of 1 cm length with a wavelength range of 200-800 nm^{-1}.

2.7. Surface Morphology

Surface evaluations were performed on mild steel sample in order to better understand their surface morphology, using ESEM Quanta 200 FEI scanning electron microscopy (SEM).

2.8. Evaluation of antimicrobial activity in vitro

The microdilution technique was used to determine the examined compound's minimum inhibitory concentration (MIC) and minimum bactericidal concentration (MIB). The process entails preparing twofold dilutions of the antimicrobial agent in a liquid growth medium spread in a 96-well microtiter plate. After dilution of the standardized microbial suspension to a scale of 0.5 McFarland, the cells were injected with a microbial inoculum made in the same medium. The 96-well microtiter plate is incubated under appropriate conditions depending on the microorganism investigated once it has been well mixed. Upon 20 hours of incubation at 37 °C, 15 L of 0.015 percent resazurin was added and incubated for a further 2 hours to detect the color changes [18].

2.9. Antioxidant activity

2.9.1. Free radical scavenging

The antioxidant capacity of the material was determined using the 1,1-diphenyl-2-picryl-hydrazyl (DPPH) procedure reported by Brand-Williams *et al.* [19]. First, 0.1 mL of the complex with different concentrations was added to 3.9 mL of a methanol solution of DPPH (1.01×10^{-2} mM). The mixture was incubated in the dark for 30 minutes before measuring absorbance at 517 nm. A mixture of 0.1 mL methanol and 3.8 mL DPPH solution was employed as a control. The decrease in absorbance shows the tested sample's ability to scavenge free radicals. Based on the percentage of DPPH radicals scavenged, the scavenging activity was determined using Equation **1** below:

$$\% \, Inhibition = [(AB - AS)/AB] \times 100 \quad (1)$$

where AB represents the absorbance of the control reaction (which contains all reagents except the test compound), and AS denotes the absorbance of the test compound. As a positive control, butylatedhydroxytoluene (BHT) was employed.

2.9.2. Ferric reducing power assay (FRAP)

The reducing power of the novel complex was determined according to the approach outlined by Oyaizu et al. [20]. 0.5 mL of varied concentrations (0-4000 g/mL) were mixed with 2.5 mL of phosphate buffer (2.5 mL, 0.2 M, pH 6.6) and potassium ferricyanide (2.5 mL, 1 percent) in 1 mL of distilled water, at 50 °C, the whole solution was incubated. 2.5 mL of 10% (w/v) trichloroacetic acid, 2.5 mL of distilled water, and 0.5 mL of a 0.1 percent (w/v) FeCl3 solution were added to the mix after 20 minutes of incubation. A UV-visible spectrophotometer was used to measure absorbance at 700 nm against a blank, and the compound's reduced power was compared to that of gallic acid, which was employed as a reference standard.

2.9.3. Phosphomolybdenum assay (PM)

According to Prieto et al. [21], the Phosphomolybdenum Assay (PM) or Total Antioxidant Capacity (TAC) was conducted. 3 mL molybdate reagent (acid sulfuric (0.6 M), sodium phosphate (28 mM), and ammonium molybdate (4 mM) were mixed with 0.3 mL sample at various concentrations (250 – 500 – 1000 g/mL). For 90 minutes, the mixture was kept at 95°C. The absorbance was measured at 695 nm, and the results were represented as (g mL^{-1}) ascorbic acid equivalents. As a positive control, glycerin was employed.

3. Results and discussion

3.1. Structure and crystal packing

The asymmetric unit of $(NH_4)_2(H_2en)_2\{V_{10}O_{28}\}.4H_2O$ (Figure 1) contains one-half decavanadate anion $[V_{10}O_{28}]^{6-}$, as denoted hereafter, one ethylenediammonium cation $(H_2en)^{2+}$, one ammonium cation $(NH_4)^+$ and two H_2O molecules.

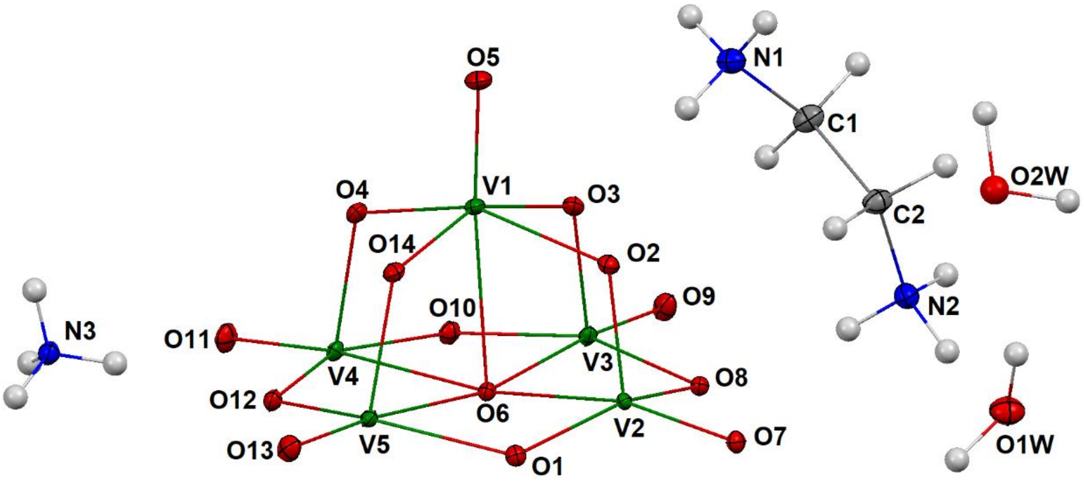

Fig. 1. ORTEP image shows the asymmetric unit of $(NH_4)_2(H_2en)_2\{V_{10}O_{28}\}.4H_2O$ with non-H atom displacement ellipsoids drawn at a probability level of 70%.

The decavanadate unit $[V_{10}O_{28}]$, of D_{2h} symmetry, is similar to the group found in hummerite [22] or in pascoite [23]. It is composed of ten deformed $\{VO_6\}$ octahedrons with shared edges, with a core $\{VO_6\}$ cluster consisting of six $\{VO_6\}$ octahedra structured in a 2*3 rectangle array and two extra $\{VO_6\}$ units on each side. Four types of oxygen atoms, bonding to the different types of vanadium, are to be distinguished: i.e., terminal oxygens (O_t) bonded to only one vanadium atom, O(µ2), O(µ3) and O(µ6) correspond to apices shared between two, three, and six vanadium atoms respectively. Average $d_{V\text{-}O}$ bond distances in the decavanadate entity are: V1-O5: 1.6086(7) Å, V3-O8: 1.9756(7) Å, V2-O6: 2.0952(7) Å, V3-O6: 2.2347(6) Å and V4-O6: 2.3155(7) Å. $[V_{10}O_{28}]$ has no remarkable geometrical features, and the bond lengths are comparable to other structures containing this oxo-cluster [24]. The rigid backbone of the $[V_{10}O_{28}]^{6-}$ anion prevents major structural changes, which might be produced by non-covalent interactions. The empirical bond length/bond number computation with Brown's function s=

$(R/1.791)^{-5.1}$ [25], where R is the V–O distance and s is the bond number, was used to assess the likelihood of protonation sites in the decavanadate anion. The computed values vary between 1.683 to 2.051 for all oxygen atoms, as shown in Table 5, omitting protonation of the decavanadate anion.

Table 5

Bond number (s) calculations for all the oxygen atoms in the $\{V_{10}O_{28}\}^{6-}$ anion.

Atom	Σs	Atom	Σs
O1	1.853	O(8)	1.787
O(2)	1.825	O(9)	1.683
O(3)	1.826	O(10)	1.728
O(4)	1.789	O(11)	1.735
O(5)	1.732	O(12)	1.778
O(6)	2.051	O(13)	1.699
O(7)	1.764	O(14)	1.693

Figure 2 illustrates the cohesion of adjacent $[V_{10}O_{28}]^{6-}$ structural units through weak electrostatic interactions engaged with the interstitial contents, i.e., ethylenediamine ($C_2H_8N_2$) referred to as “en”, water molecules “H_2O” and ammonium “NH_4^+”. The strong O–H•••O and N–H•••O interactions with the $(H_2en)^{2+}$ and H_2O entities are primarily mediated by the O(3), triply connected, and O(2), double-linked oxygen atoms, while the terminal oxygen (O_t) is involved mainly in the weakest N–H···O interactions with $(NH_4)^+$. Each $\{V_{10}O_{28}\}^{6-}$ anion is surrounded by two $(H_2en)^{2+}$ cations. $\{V_{10}O_{28}\}^{6-}$ anion behaves as reported in [26]. Table 4 summarizes the significant H-Bonds linking the $\{V_{10}O_{28}\}^{6-}$ anions to the interstitial entities $(H_2en)^{2+}$, $(NH_4)^+$ and H_2O.

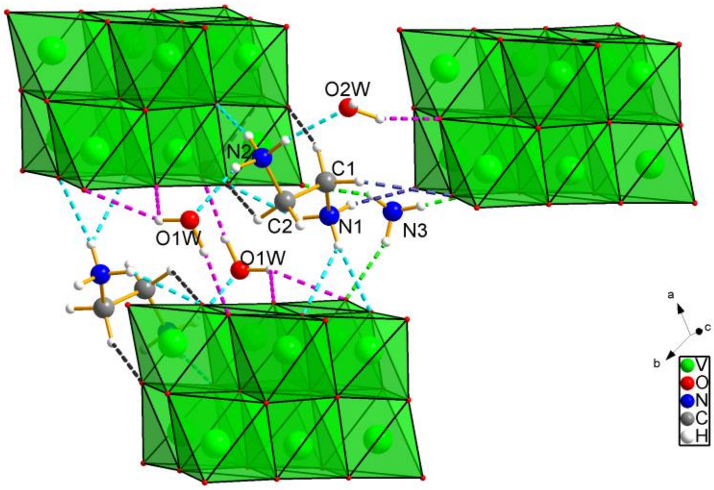

Fig. 2. Illustration of the framework of $(NH_4)_2(H_2en)_2\{V_{10}O_{28}\}.4H_2O$ showing hydrogen bonds between the clusters.

3.2. Infrared spectroscopy

The infrared spectrum of $(NH_4)_2(H_2en)_2\{V_{10}O_{28}\}.4H_2O$ is depicted in Figure 3 and Table 6 lists the suggested assignments for several significant bands. Based on the decavanadate-based coordination polymers description [27], the stretching mode of the terminal V-O bonds may be shown in the spectrum at 930 cm^{-1}, where two strong bands can be seen. The bands at 508 and 448 cm^{-1} are attributed to the symmetric V–O–V bridge, whereas the characteristics at 810, 722 cm^{-1} are related to the bridging anti-symmetric V–O–V vibrations. The presence of the organic ethylenediammonium cation is confirmed by the stretching C-N bands at 1043, 1079 and 2419 cm^{-1}, as by the vibrational bands at 3160-3030 cm^{-1} and 1600 cm^{-1} that correspond, respectively, to N-H bending and the H-N-H scissoring. The bands 2757, 2932 and 2117 cm^{-1} are related to the C-H stretching [28]. The broad band at 1404 cm^{-1} might be assigned to the N-H bending vibration of the ammonium cation. Further, the presence of water molecules is confirmed by the 3517-3238 cm^{-1} and 1807 cm^{-1} bands [29].

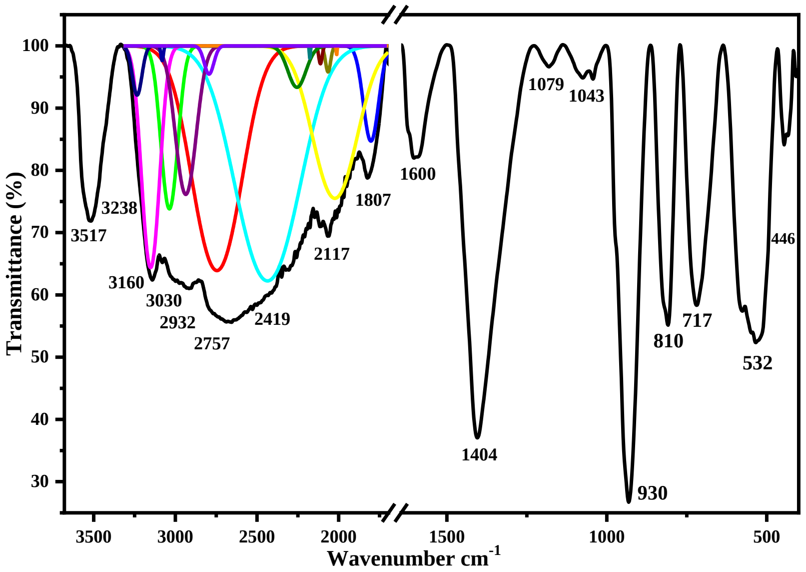

Fig. 3. Infrared spectrum of $(H_2en)_2(NH_4)_2\{V_{10}O_{28}\}.4H_2O$.

Table 6.

Infrared bands and assignments for complex **1**.

Band (cm^{-1})	~930	810, 717, 532	3160-3030; 1600	1043, 1079	1807; 3517-3238	1404
Assignment	The stretching of the terminal V-O	Asymmetric and symmetric stretching vibrations of V-O-V	N-H (en) bending H-N-H scissoring	The stretching C-N	H-O-H bending O-H stretching	N-H (NH_4) bending

3.3. Thermal analysis

The thermal decomposition of $(NH_4)_2(H_2en)_2\{V_{10}O_{28}\}.4H_2O$ was performed under air atmosphere and exhibits a total weight loss of 25% (Figure 4). The mass loss observed in the 100-500 °C temperature range corresponds to three consecutive weight losses around 100, 160 and 260 °C. The initial phase weight loss 12.2 % correlates to the water molecules' departure, ammonium ion and ½O_2 (calcd. 10.8 %). Next step corresponds to the loss of the ethylenediamonium organic cation (exp. 9.1 %, calcd. 10.4 %) and further weight loss beyond 260 °C relates to decavanadate cluster decomposition. Actually, the calculated value of the loss weight of the last step agrees to the degradation of decavanadate cluster and the formation of (V_2O_5) and (V_3O_7) (exp. 78.7 %, calcd. 78.1 %) [30].

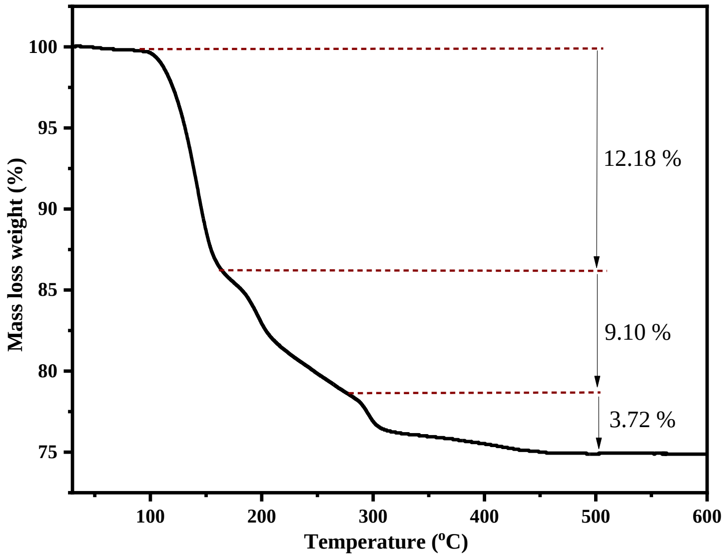

Fig. 4. Thermographic curve of $(H_2en)_2(NH_4)_2\{V_{10}O_{28}\}.4H_2O$.

According to TGA analysis, and to confirm the nature of the final product after calcination, temperature dependent in situ XRD data were acquired at room temperature and 450 °C, as shown in Figure 5. The pattern at RT was quite similar to the pattern that had been simulated using the coordinates from the single-crystal investigation of $(NH_4)_2(H_2en)_2\{V_{10}O_{28}\}.4H_2O$. However, at 450 °C the structure changes, while keeping the crystallinity of the sample and presenting a different product. The 450 °C XRD pattern showed the characteristic peaks of V_2O_5 and V_3O_7 as well [31], approving the TGA calculation results, with a small unidentified diffraction peak.

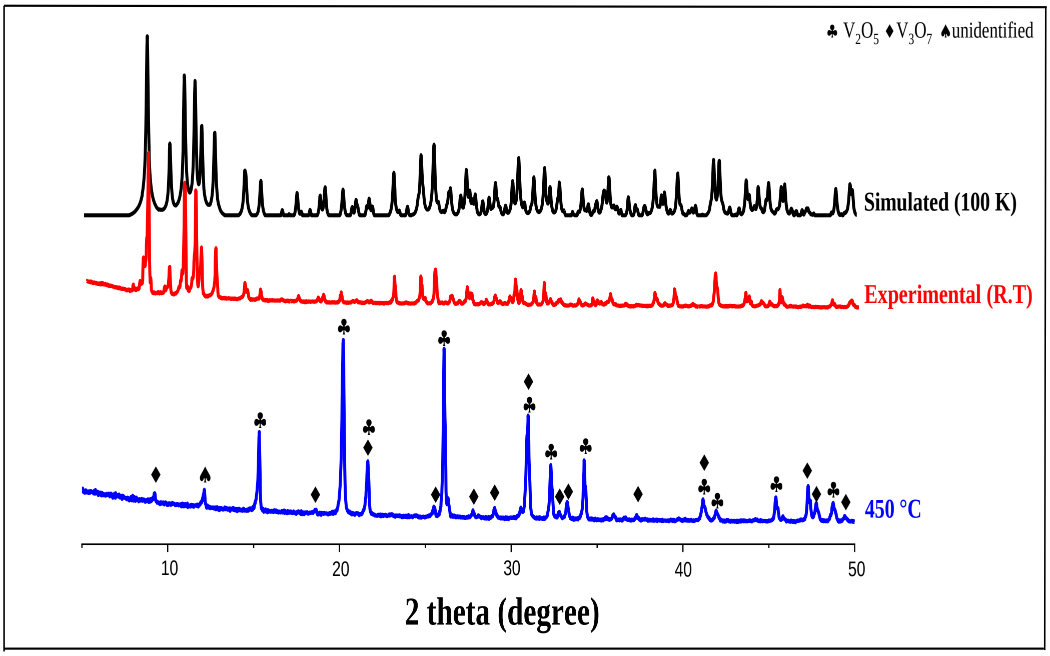

Fig. 5. The simulated, experimental and the thermal treatment at 450°C XRD pattern of $(NH_4)_2(H_2en)_2\{V_{10}O_{28}\}.4H_2O$.

3.4. Speciation vs. corrosion inhibition

3.4.1. Changes in vanadate speciation with pH

Because of a lack of understanding of speciation, the complexity of vanadate hydrolysis in aqueous solutions, and the occurrence of metastable equilibria, the results of known investigations on corrosion inhibition by vanadates are clouded. The major goal of this part is to figure out which vanadate oligomer provides the best mild steel corrosion resistance in two aggressive solutions (1 M HCl and 3 percent NaCl). We used pH measurements, ultraviolet-visible spectroscopy, PP and EIS measurements, and scanning electron microscopy initially. According to the literature, small changes in solution pH may have a large effect on vanadate speciation [32,33]. $(H_2en)_2(NH_4)_2\{V_{10}O_{28}\}.4H_2O$ is a colorless complex when dissolved in 1 M HCl, the solution has a pH of 0.315. Whereas, when dissolved in 3% NaCl, the solution turned yellow and its pH is of 7.6, as shown in Figure 6.

Fig. 6. Photograph of $(H_2en)_2(NH_4)_2\{V_{10}O_{28}\}.4H_2O$ dissolved in 3% NaCl (Left) and 1 M HCl (Right).

3.4.2. UV-Visible spectroscopy measurements

According to Aureliano, the presence of $[V_{10}O_{28}]^{6-}$ anions is responsible for the yellow color of the solution [34]. Actually, the yellow color of solutions containing V^{5+} ($3d^0$) ions are due to electrons transfer from the oxygen bonding orbitals to the vacant vanadium d orbitals. These charge transfer bands move towards the UV-region when the crystal field splitting of d orbitals decreases [35].

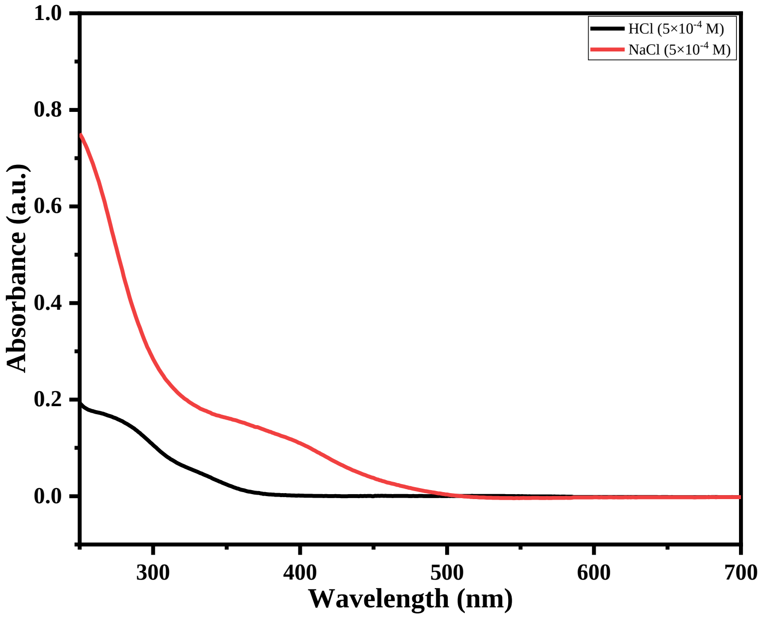

Fig. 7. UV-visible spectra of $(H_2en)_2(NH_4)_2\{V_{10}O_{28}\}.4H_2O$, measured at 25 °C, in HCl (5×10^{-4} M) (black) and NaCl (5×10^{-4} M) (red).

Electronic absorption spectra of were taken with a UV-Vis spectrometer within the range [200-800 nm] at room temperature of $(H_2en)_2(NH_4)_2\{V_{10}O_{28}\}.4H_2O$ in both 1 M HCl and 3% NaCl at the same concentration of 5×10^{-4} M. As shown in Figure 7, the 280 nm (black line) and 391 nm (red line) bands are attributed to the V^{5+} tetrahedrally coordinated in monovanadates and octahedrally in decavanadates, respectively [36-38].

3.4.3. EIS measurements of vanadate solution

The electrochemical behavior of clear solution containing monovanadates and orange solution containing decavanadates at the mild steel interface was clearly distinctive. The impedance spectra given in the Nyquist representation are illustrated in Figure 8. Without any calling, upon the simulation of these spectra, with equivalent electrical circuits, just only on the basis of visual inspection, the spectrum reveals that, corrosion inhibition of MS by monovanadates was very rapid and approximately 30 min were required to develop a layer. The adsorption of the inhibitor blocked the reactive sites on MS surface signifying the increase of diameter of the loop when compared to the blank 1 M HCl. In contrast, yellow solution was shown to be poor inhibitor, after one hour of immersion of MS under open circuit potential, the yellow solution exhibits any protection of surface, which is reflected by the superposition of the loop that contains the inhibitor with the blank 3% NaCl.

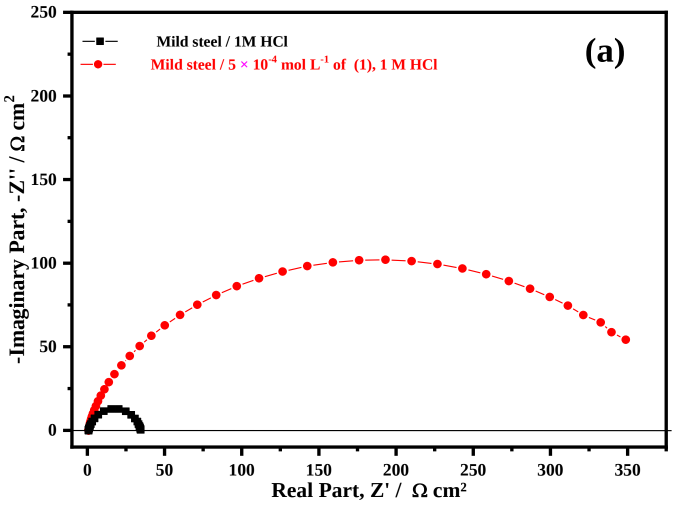

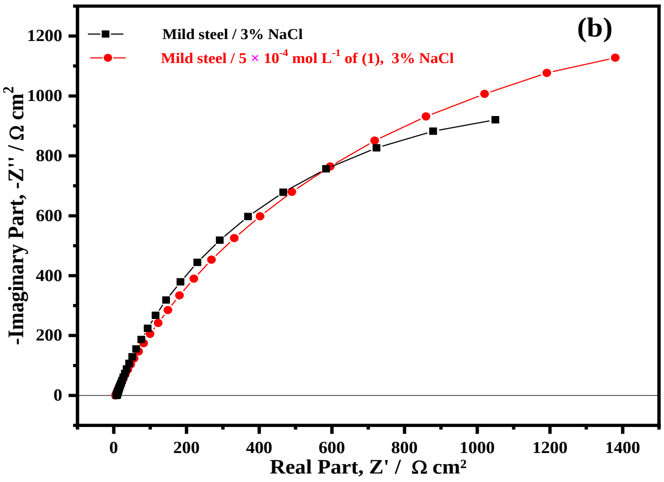

Fig. 8. Nyquist plots of the mild steel matrix in: (**a**) 1 M HCl, (**b**) 3% NaCl with 5×10^{-4} M of $(H_2en)_2(NH_4)_2\{V_{10}O_{28}\}.4H_2O$ at 25 °C.

3.4.4. Corrosion morphology of mild steel in vanadate solution

To observe the action of the two solutions on the topography surface of MS, scanning electron microscopy was used. Figure 9 shows the SEM micrographs of MS specimen exposed to 1 M HCl and 3% NaCl during 24 h, in which the complex $(H_2en)_2(NH_4)_2\{V_{10}O_{28}\}.4H_2O$ was dissolved. The effects of decavanadates are dramatic on MS surface; very large alterations on the surface are evident, indicating severe corrosion of specimen (Figure 9a). Rather Figure 9b indicates that in the presence of $(H_2en)_2(NH_4)_2\{V_{10}O_{28}\}.4H_2O$ in clear solution, the rate of corrosion is suppressed, as can be seen from the decrease of the corroded area. The surface is covered by a thin layer of monovadates molecules, which effectively controls the dissolution of MS.

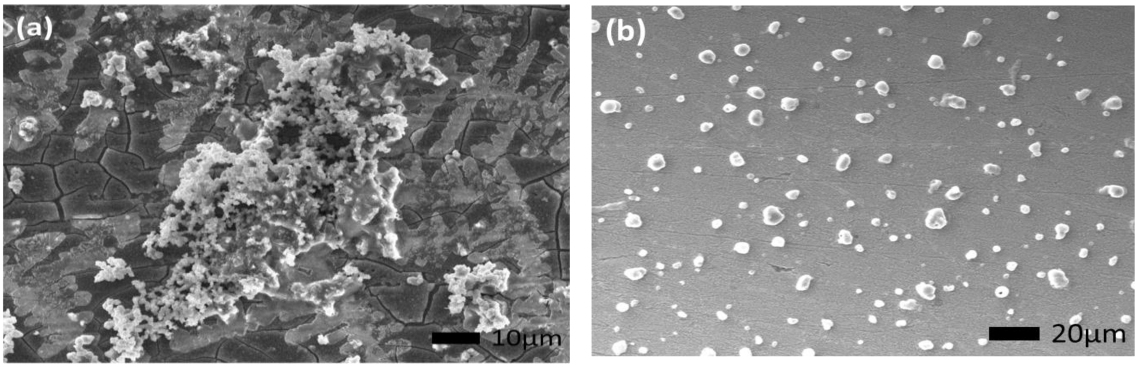

Fig. 9. SEM micrographs of the MS surface after 24 h immersion: (**a**) in 3% NaCl at 5×10^{-4} M of $(H_2en)_2(NH_4)_2\{V_{10}O_{28}\}.4H_2O$. (**b**) in 1 M HCl at 5×10^{-4} M of the title complex.

Monovanadates were only found in clear metavanadate solutions, but decavanadates were always present in yellow solutions. The latter, which contained 3 percent NaCl at pH = 7.6, showed no appreciable inhibition, and any rise in decavanadate content was only harmful. The clear solution containing monovanadates, on the other hand, demonstrated substantial inhibition.

3.5. Electrochemical study of the clear solution

3.5.1. PP measurements

The PP measurements represent an essential method to gather details about the kinetics of corrosion system being investigated. Figure 10 presents the results of the effect of $(H_2en)_2(NH_4)_2\{V_{10}O_{28}\}.4H_2O$ in the clear solution on the anodic and cathodic polarization behavior of MS in 1 M HCl at 25 °C, using recorded Tafel plots after half an hour of immersion at the open-circuit potential.

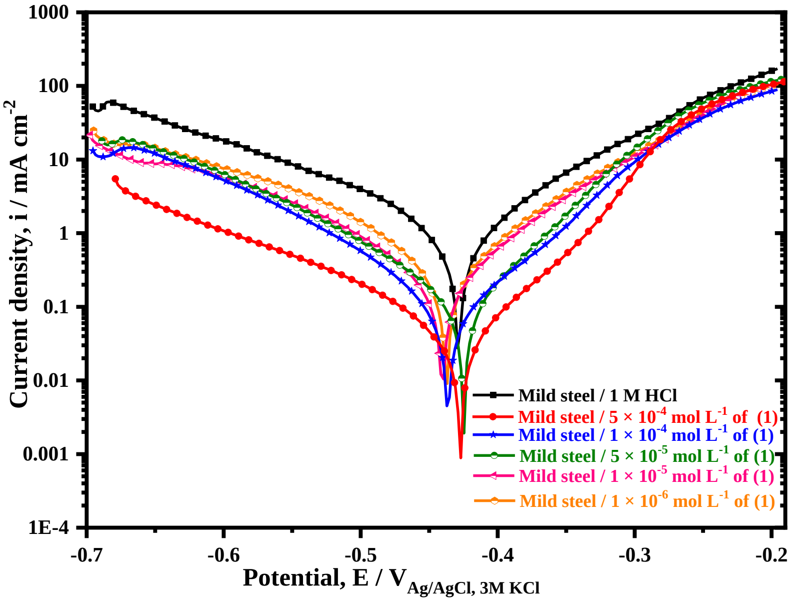

Fig. 10. PP curves of mild steel in 1 M HCl at 25 °C and different concentrations of $(H_2en)_2(NH_4)_2\{V_{10}O_{28}\}.4H_2O$.

It can be concluded from these results (Figure 10) that both anodic iron dissolution and cathodic hydrogen evolution reaction were inhibited after the addition of $(H_2en)_2(NH_4)_2\{V_{10}O_{28}\}.4H_2O$ in 1 M HCl solution. The inhibition of these reactions was more pronounced on increasing the concentration of the title complex, ranging from 1×10^{-6} to 5×10^{-4} mol L^{-1}. From cathodic branches, a broad linearity is clearly shown in the absence as well as in the presence of different concentrations of $(H_2en)_2(NH_4)_2\{V_{10}O_{28}\}.4H_2O$. This behavior confirms that the reduction of hydrogen takes place at the mild steel surface by charge transfer mechanism [39]. In the other side, the anodic branches exhibit almost an absence of Tafelian behavior and the inhibition mode remains dependent on the electrode potential. In addition, the title complex influences the anodic reaction only at over potentials more negative than -300 $mV_{Ag/AgCl}$. Over this potential, the title compound assigns no inhibiting effect, and thereby the anodic branches recorded in the presence of the title compound joined the blank. This can be explained by desorption of the studied complex "molecules" from the formed film. The desorption potential is a common term for this potential [40].

As stated above, the anodic dissolution of mild steel is not activation controlled. Therefore, according to the shape of the anodic curves, it will be erroneous to extract the anodic Tafel slopes $ß_a$ in order to evaluate the corrosion densities [41]. As a result, by extrapolating solely the right-hand side of Tafel cathodic to the corrosion potential, corrosion current densities can be determined. The extraction of electrochemical parameters from the polarization curves was carried out using two methods: Tafel, and Stern & Geary (S&G), which use these curves differently, depending on the range potentials $E_{corr} \pm 250$ $mV_{Ag/AgCl}$, $E_{corr} \pm 25$ $mV_{Ag/AgCl}$, respectively. The values of i_{corr}, E_{corr}, cathodic Tafel slopes $ß_c$ and $\eta\%$ issued from linear Tafel segments of cathodic curves and R_p obtained by S&G method are regrouped in Table 7. The data were fitted by using Tafel Fit analysis tool based on Linear Square method used along with

EC-Lab software. In this case the inhibition efficiency derived from Tafel method signified by η_{Tafel} %, is calculated using the Equation **2**, as follows:

$$\eta_{Tafel}\,\% = \left(\frac{i_{corr} - i_{corr/inh}}{i_{corr}} \right) \times 100 \qquad (2)$$

where: $i_{corr/inh}$ and i_{corr} represent the corrosion current density values, with and without $(H_2en)_2(NH_4)_2\{V_{10}O_{28}\}.4H_2O$, respectively.

The inhibition efficiency of S&G method, given by $\eta_{S\&G}$%, is calculated from the polarization resistance, using the following Equation **3**:

$$\eta_{S\&G}\,\% = \left(\frac{R_{p/inh} - R_p}{R_{p/inh}} \right) \times 100 \qquad (3)$$

where: R_P and $R_{P/inh}$ are the polarization resistances of the MS without and with addition of the studied complex, respectively.

Table 7

Electrochemical parameters obtained from the PP curves of the MS immersed in 1 M HCl at different concentrations of **1**, and at 25 °C.

	Tafel fit				R_p fit		
Electrode/electrolyte interface	E_{corr} $mV_{Ag/AgCl}$	i_{corr} $\mu A\ cm^{-2}$	$ß_c$ $mV\ dec^{-1}$	η_{Tafel} %	E_{corr} $mV_{Ag/AgCl}$	R_P $\Omega\ cm^2$	$\eta_{S\&G}$ %
MS / 1 M HCl	-428.8	1439.9	-156.8	-	-428.7	23.5	-
MS / 1×10^{-6} M of **1**	-437.7	792.60	-165.6	44.9	-437.5	60.6	61.2
MS / 1×10^{-5} M of **1**	-440.4	281.06	-123.1	80.5	-443.1	84.7	72.3
MS / 5×10^{-5} M of **1**	-425.2	187.27	-114.5	87.0	-425.6	132.0	82.2
MS / 1×10^{-4} M of **1**	-436.8	182.90	-112.3	87.3	-435.8	180.0	86.0
MS / 5×10^{-4} M of **1**	-427.1	70.89	-146.1	95.1	-428.4	433.0	94.6

with 1 = $(H_2en)_2(NH_4)_2\{V_{10}O_{28}\}.4H_2O$.

Table 7 shows that the corrosion current density i_{corr} decreases considerably in the presence of $(H_2en)_2(NH_4)_2\{V_{10}O_{28}\}.4H_2O$ with rise of concentrations and reaches a minimum value of 70.89 µA cm^{-2} at 5×10^{-4} M. However, the R_p values have an opposite trend with i_{corr}. Consequently, the inhibition efficiency, calculated from Tafel and S&G methods, increases to rich 95.1% and 94.6%, respectively.

However, there is no definite trend in the shift of E_{corr} values at different concentrations of the complex. The corrosion potential of the MS shifts, in the range, from -11 to 3 mV relative to the uninhibited solution. Therefore, it has been proposed from the literature that if the E_{corr} shift upon addition of the inhibitor is greater than 85 mV relative to the corrosion potential of the blank [42], then the inhibitor can be classified as either cathodic or anodic type and if the shift is less than 85 mV, then the inhibitor can be considered as mixed type. Consequently, the results obtained indicate that $(H_2en)_2(NH_4)_2\{V_{10}O_{28}\}.4H_2O$ acts as mixed type inhibitor with predominant cathodic effectiveness. Also, the cathodic Tafel line values $ß_c$, change with the addition of $(H_2en)_2(NH_4)_2\{V_{10}O_{28}\}.4H_2O$ suggesting that the mechanism of hydrogen evolution reaction is changed in the presence of the title compound. This behavior is explained by Bockris and Srinivansan that the change in the values of $ß_c$ can be ascribed to the thickening of the electric double layer due to the adsorbed inhibitor molecules [43].

It can be concluded that the inhibiting efficiencies calculated by the S&G method show the same trend as those determined by extrapolating the Tafel cathodic straight lines to the corresponding corrosion potentials.

3.5.2. EIS measurements

To confirm the results extracted from PP measurements and to acquire more information on the inhibition mechanism, obtained for the MS electrode after 30 min of immersion at the corrosion potential in the 1 M HCl with and without $(H_2en)_2(NH_4)_2\{V_{10}O_{28}\}.4H_2O$, Figure 11 shows the impedance diagrams, given in both Nyquist and Bode coordinates.

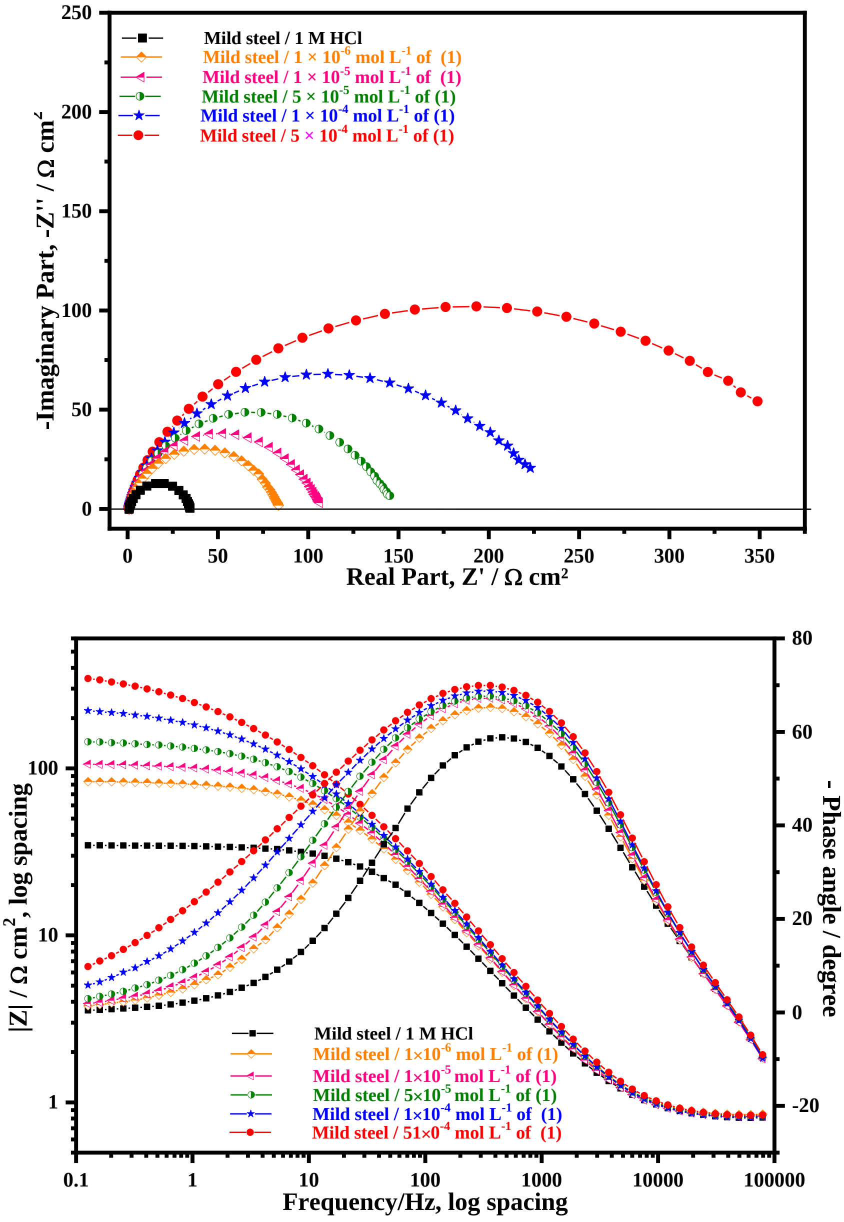

Fig. 11. Mild steel Nyquist and Bode graphs in 1 M HCl without and with various amounts of $(H_2en)_2(NH_4)_2\{V_{10}O_{28}\}.4H_2O$ at 25 degrees Celsius.
with 1 = $(H_2en)_2(NH_4)_2\{V_{10}O_{28}\}.4H_2O$.

All Nyquist spectra show only one loop. In addition, ideal capacitance behavior is not observed at solid interface electrode [44] manifested as a related depression of Nyquist-plot semicircles with increasing the $(H_2en)_2(NH_4)_2\{V_{10}O_{28}\}.4H_2O$ inhibitor concentration. The deviation from ideal capacitance behavior refers to a frequency-dependent phase angle and the non-ideal behavior can be represented by a constant phase element CPE. This dispersion of the capacitance at solid electrodes depends strongly on the status of the electrode surface. With this visual inspection, the choice was made on $\{R_s+CPE_{dl}/R_{ct}\}$ circuit shown in Figure 12 (a) to model the interface and extract the electrochemical parameters in order to fully understand the effect of $(H_2en)_2(NH_4)_2\{V_{10}O_{28}\}.4H_2O$ on MS surface. Nevertheless, it was observed that with increasing concentration of $(H_2en)_2(NH_4)_2\{V_{10}O_{28}\}.4H_2O$, this model does not perform a good fit of the data neither in Nyquist, nor in Bode representations.

However, from the Bode plots, the width of the Gaussian (φ-$\log f$) obtained in the presence of different concentrations of $(H_2en)_2(NH_4)_2\{V_{10}O_{28}\}.4H_2O$ is significantly larger than that obtained in 1 M HCl alone. This finding states the occurrence of a second time constant, although poorly separated from that of the charge transfer in the presence of different concentrations of the title compound. This second phenomenon of relaxation or time constant is generally attributed to the presence of an additional obvious process on MS surface. This simple qualitative analysis confirms the formation of a barrier film that prevents the infiltration of corrosive species at the metal/solution interface. After examination of several electrical circuits, only $\{R_s+CPE_{dl}/(R_{ct}+CPE_f/R_f)\}$, shown in Figure 12 (b), which provides the best superposition between experimental and theoretical data.

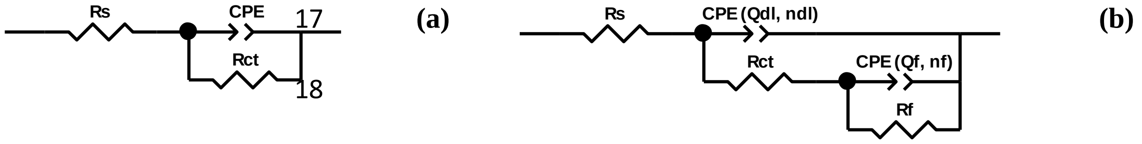

Fig. 12. Equivalent electric circuit models.

Figure 13 gives a detailed comparison between the simulations with the two circuits mentioned above. Furthermore, the obtained results have a physical meaning. R_s represents the solution resistance, R_{ct} is the charge transfer resistance and CPE_{dl} represents the capacitance of the high frequency semicircle that can be attributed to the charge transfer process. R_f represents the resistance of the adsorbed inhibitor and CPE_f is the capacitance of the inhibitor film due to the inhibitor's adsorption onto the MS surface.

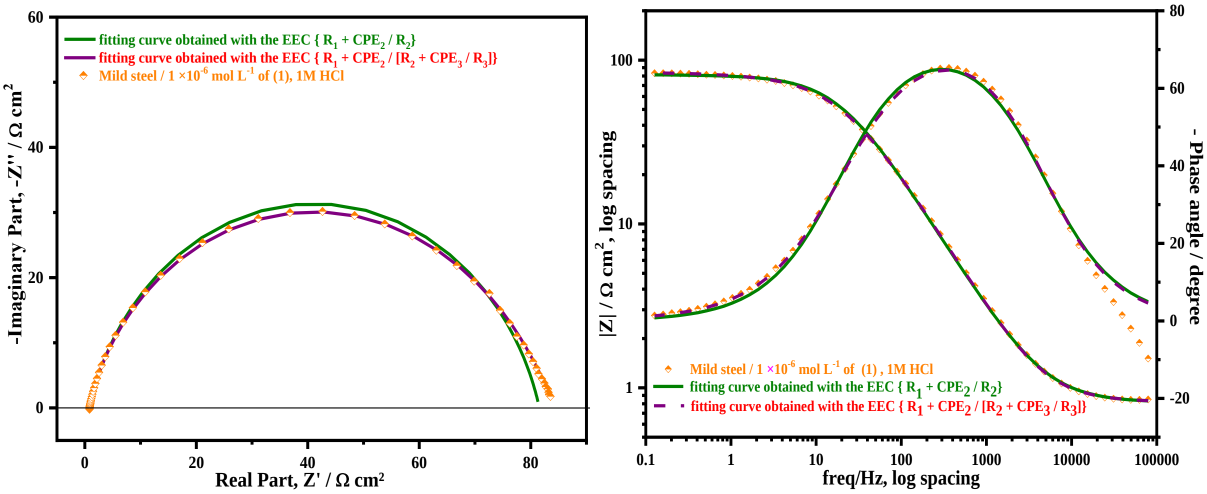
fitting curve obtained with the EEC { R_1 + CPE_2 / R_2}
fitting curve obtained with the EEC { R_1 + CPE_2 / [R_2 + CPE_3 / R_3]}
Mild steel / 1 ×10^{-6} mol L^{-1} of (1), 1M HCl
-Imaginary Part, -Z'' / Ω cm^2
Real Part, Z' / Ω cm²
0
20
40
60
80
|Z| / Ω cm^2, log spacing
- Phase angle / degree
freq/Hz, log spacing
Mild steel / 1 ×10^{-6} mol L^{-1} of (1), 1M HCl
fitting curve obtained with the EEC { R_1 + CPE_2 / R_2}
fitting curve obtained with the EEC { R_1 + CPE_2 / [R_2 + CPE_3 / R_3]}
0.1
1
10
100
1000
10000
100000
-20
0
20
40
60
80

1

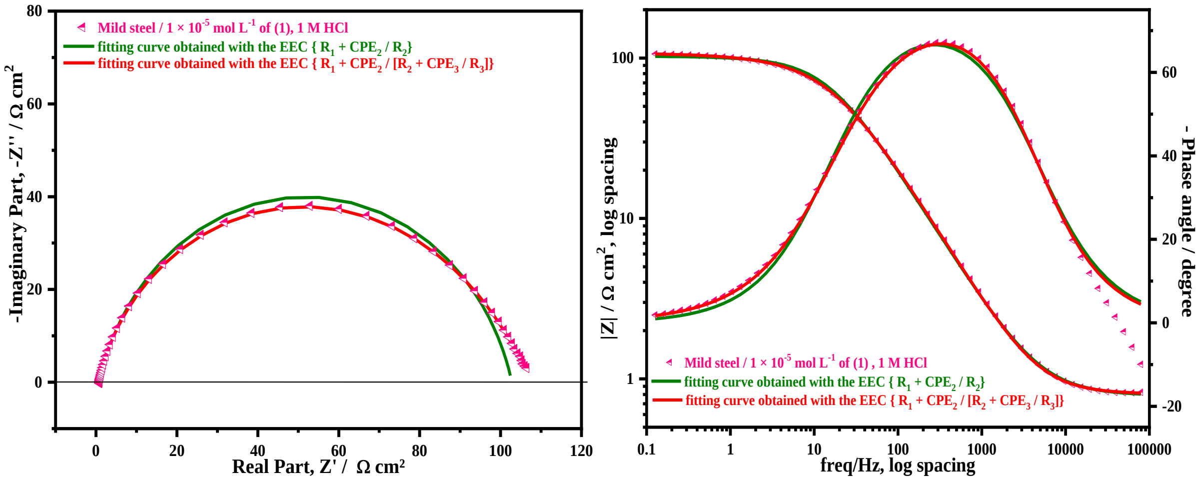
Mild steel / 1 × 10^{-5} mol L^{-1} of (1), 1 M HCl
fitting curve obtained with the EEC { R_1 + CPE_2 / R_2}
fitting curve obtained with the EEC { R_1 + CPE_2 / [R_2 + CPE_3 / R_3]}
-Imaginary Part, -Z'' / Ω cm^2
Real Part, Z' / Ω cm²
0
20
40
60
80
100
120
|Z| / Ω cm^2, log spacing
- Phase angle / degree
freq/Hz, log spacing
Mild steel / 1 × 10^{-5} mol L^{-1} of (1), 1 M HCl
fitting curve obtained with the EEC { R_1 + CPE_2 / R_2}
fitting curve obtained with the EEC { R_1 + CPE_2 / [R_2 + CPE_3 / R_3]}
0.1
1
10
100
1000
10000
100000
-20
0
20
40
60

2

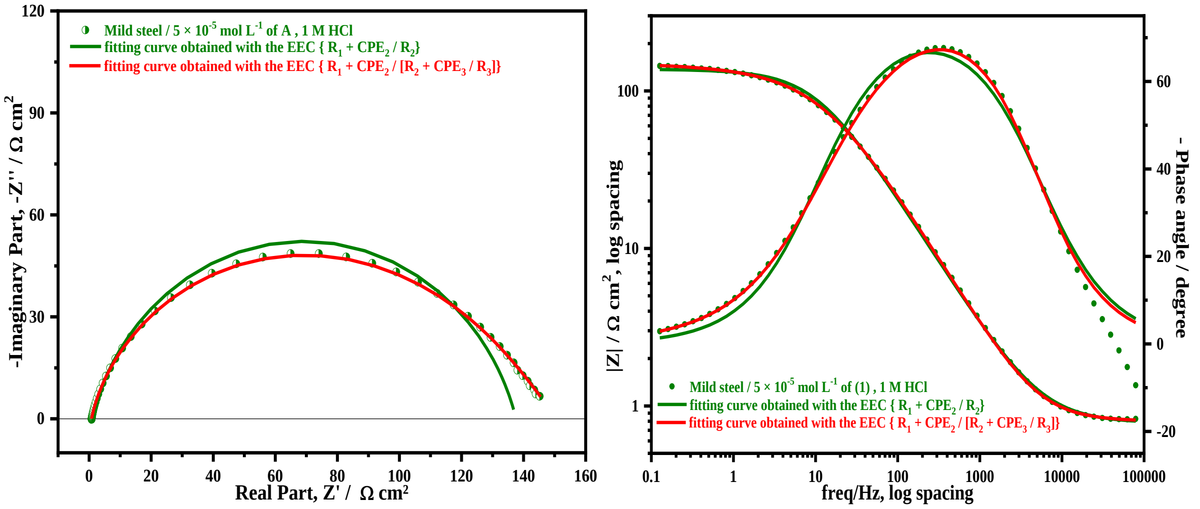
Mild steel / 5 × 10^{-5} mol L^{-1} of A , 1 M HCl
fitting curve obtained with the EEC { R_1 + CPE_2 / R_2}
fitting curve obtained with the EEC { R_1 + CPE_2 / [R_2 + CPE_3 / R_3]}
-Imaginary Part, -Z'' / Ω cm^2
Real Part, Z' / Ω cm²
0
30
60
90
120
0
20
40
60
80
100
120
140
160
|Z| / Ω cm^2, log spacing
- Phase angle / degree
freq/Hz, log spacing
Mild steel / 5 × 10^{-5} mol L^{-1} of (1) , 1 M HCl
fitting curve obtained with the EEC { R_1 + CPE_2 / R_2}
fitting curve obtained with the EEC { R_1 + CPE_2 / [R_2 + CPE_3 / R_3]}
0.1
1
10
100
1000
10000
100000
-20
0
20
40
60

3

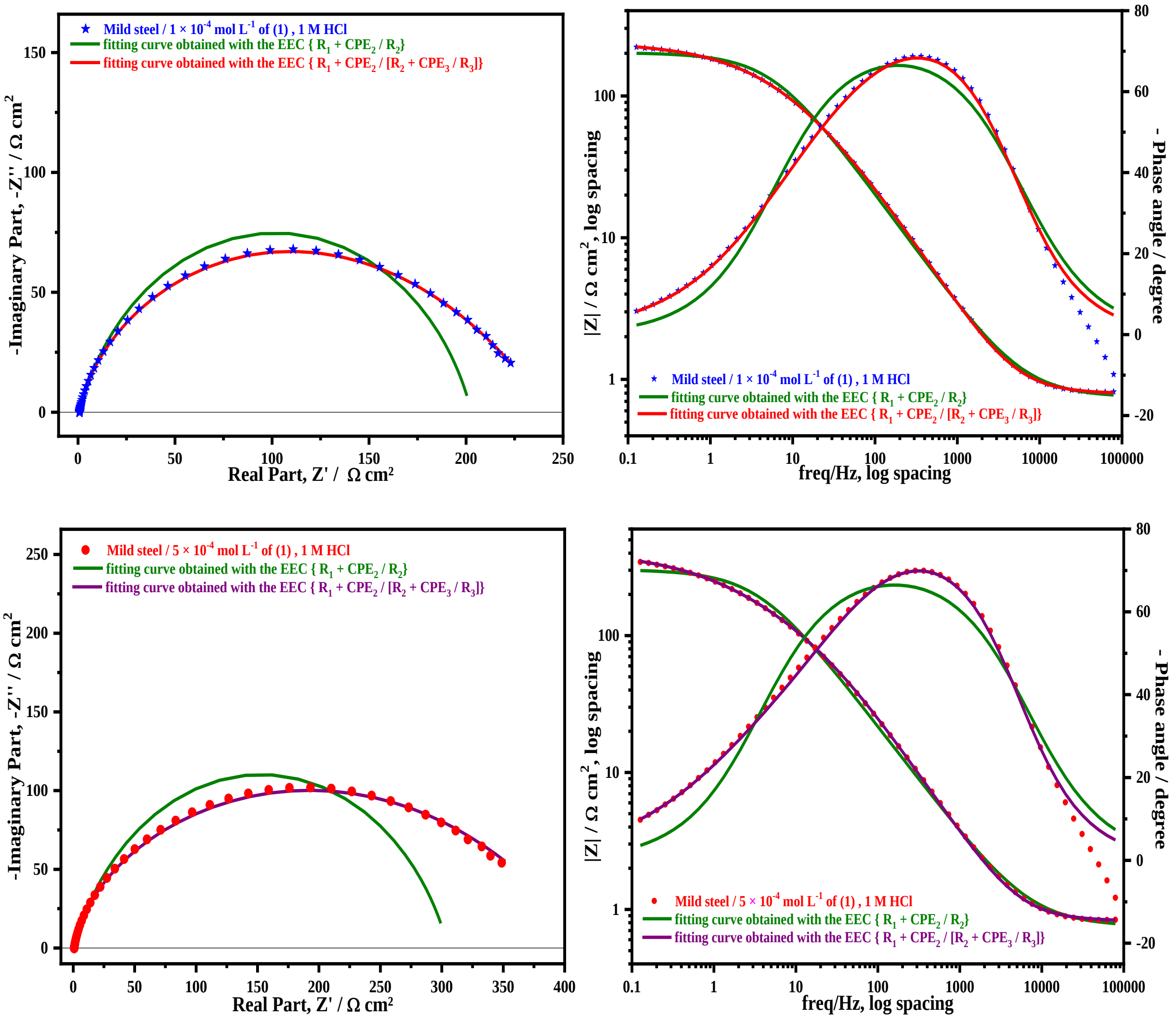

Fig. 13. Nyquist and Bode diagrams simulated by {R_s+CPE_{dl}/R_{ct}} and {$R_s+CPE_{dl}/(R_{ct}+CPE_f/R_f)$} at different concentrations of $(H_2en)_2(NH_4)_2\{V_{10}O_{28}\}.4H_2O$.
with 1 = $(H_2en)_2(NH_4)_2\{V_{10}O_{28}\}.4H_2O$.

When the experimental error structure remains unknown, the statistical value χ^2 cannot be used to evaluate the quality of a regression. Another important parameter to judge the goodness of the fit is the ratio $\chi^2/|Z|$. Indeed, the appropriate set of parameter values are the values that yield the lower $\chi^2/|Z|$ value, which gives an estimation of the distance between the real data and simulated data weighted on the value of $|Z|$. χ^2 is expressed by Equation **4** below as stated in the literature [45]:

$$\chi^2 = \sum_{i=1}^{n} \frac{|Z_{meas}(i) - Z_{model}(f_i, param)|^2}{|Z_{meas}(i)|} \quad (4)$$

where: $Z_{\mathrm{meas}}(i)$ is the measured impedance at the fi frequency; Z_{model} (fi, param) is function of the chosen model and param is the model parameters (R_s, R_{ct},Q_{dl} ,R_f, Q_f).

The electrochemical impedance parameters for MS in 1 M HCl in the presence of different concentrations of $(H_2en)_2(NH_4)_2\{V_{10}O_{28}\}.4H_2O$ are reported in Table 8. The values used to determine the efficiency of the inhibitor are the values of the polarization resistance calculated by the following equation ($R_P = R_{ct} + R_f$). The inhibition efficiency is calculated based on Equation **5**:

$$\eta_{EIS}\,\% = \left(\frac{R_{p/inh} - R_p}{R_{p/inh}}\right) \times 100 \qquad (5)$$

Table 8

EIS parameters and inhibition efficiency for mild steel in 1 M HCl at different concentrations of **1**.

Electrode/electrolyte interface	R_S	Q_{dl}	n_{dl}	R_{ct}	Q_f	n_f	R_f	R_p	η_{EIS}%	$\chi^2/\lvert Z\rvert$
MS / 1 M HCl	0.7765	280.0	0.8232	30.17	512.3	0.6501	3.792	33.96	-	0.336
MS / 1×10^{-6}M of **1**	0.8182	166.5	0.8641	38.17	708.7	0.5295	45.66	83.83	60	0.255
MS / 1×10^{-5}M of **1**	0.8010	155.6	0.8774	44.07	765.8	0.5088	63.40	107.78	68	0.259
MS / 5×10^{-5}M of **1**	0.7971	148.7	0.8743	51.34	905.3	0.4928	98.90	150.24	77	0.255
MS / 1×10^{-4}M of **1**	0.7899	137.9	0.8816	59.90	998.1	0.5085	182.80	242.70	86	0.269
MS / 5×10^{-4}M of **1**	0.8201	121.1	0.8871	83.36	1069	0.5067	335.10	418.46	92	0.248

R_s, R_{ct}, R_f and R_p in $\Omega\ cm^2$. Q_{dl} *and* Q_f *in* $\mu F\ s^{n-1}\ cm^{-2}$.
with 1 = $(H_2en)_2(NH_4)_2\{V_{10}O_{28}\}.4H_2O$.

Table 8 shows clearly that R_{ct} and Q_{dl} values have opposite trend at the whole concentration range. A large R_{ct} is associated with a slower corroding system [46,47]. Furthermore, the decrease in the Q_{dl} with increase in $(H_2en)_2(NH_4)_2\{V_{10}O_{28}\}.4H_2O$ concentration may be attributed to the formation of a protective layer on MS surface [48]. The increase of n_{dl} value after addition of the title compound in the corrosive solution can corroborate this assumption. Indeed, the value of n_{dl} grows as well 0.8871, when compared to that obtained in pure 1 M HCl of 0.8232. This can be attributed to a certain decrease in the initial surface homogeneity resulting from the adsorption of the title complex “molecules” on the most active adsorption centers at MS interface [46]. The resistance R_f has high values compared to R_{ct} values (the total resistance R_p is dominated by R_f and increases significantly with the $(H_2en)_2(NH_4)_2\{V_{10}O_{28}\}.4H_2O$ concentration. However, the values of Q_f have the same trend as those of R_f in the whole concentration range, while almost no change is observed in the value of n_f with lower than those of n_{dl}, probably related to the energy dissipation in the adsorbed layer [49].

It is clearly evident that increasing the concentration of the inhibitor enhances R_p, and thus improves the efficiency of the inhibition until reaching their maximum value at 5×10^{-4} M to 92%. This value suggests that inhibitors function by adsorption at the metal/solution interface, leading to a protective film on the metal surface.

3.6. Biological activities

3.6.1. Antimicrobial tests

The new hybrid decavanadate compound $(H_2en)_2(NH_4)_2\{V_{10}O_{28}\}.4H_2O$ was evaluated for antibacterial efficacy against two Gram-(*Pseudomonas aeruginosa* ATCC27653 and *Escherichia coli* CIP5412) and two Gram+ (*Bacillus subtilis* ILP1428B, *Staphylococcus aureus* CIP543154) strains. Table 9 shows MIC (Minimum Inhibitory Concentration) and MBC (Minimum Bactericidal Concentration) by ppm. The compound showed the highest inhibition activity against *P. aeruginosa* (625 ppm), *B. subtilis* (1250 ppm), and *E. coli* with 2500 ppm, although there was no substantial action against *S. aureus* CIP.

Table 9

The inhibition activity and the bactericidal activity of complex **1**.

	MIC (ppm)	MBC (ppm)
B. subtilis	1250	5000
P. aeruginosa	625	ND
E. coli CIP	2500	ND
S. aureus CIP	No activity	-

with 1 = $(H_2en)_2(NH_4)_2\{V_{10}O_{28}\}.4H_2O$.

On the other hand, the compound displayed a lower bactericidal activity with *B. subtilis* (5000 ppm), and it was not determined (ND) for *P. aeruginosa* and *E. coli* CIP. All these results show a weak activity compared to similar decavanadate complexes [50], chitosan-$Ca_3V_{10}O_{28}$, and $(NH_4)_6V_{10}O_{28}$, that manifest good bactericidal activity with *S. aureus* and *E. coli* (Table 10).

Table 10

Antibacterial activity of $(NH_4)_2(H_2en)_2\{V_{10}O_{28}\}.4H_2O$, $(NH_4)_6V_{10}O_{28}$, and chitosan-$Ca_3V_{10}O_{28}$.

Microorganisms	Antibacterial, MIC (ppm)		
	$(NH_4)_2(H_2en)_2\{V_{10}O_{28}\}.2H_2O$	$(NH_4)_6V_{10}O_{28}$	Chitosan-$Ca_3V_{10}O_{28}$
Staphylococcus aureus	No activity	50	12.5
Escherichia coli	2500	50	12.5

with 1 = $(H_2en)_2(NH_4)_2\{V_{10}O_{28}\}.4H_2O$.

3.6.2. Antioxidant tests

The DPPH test is one of the most often used procedures for determining antioxidant activity. Accordingly, an antioxidant reacts with DPPH free radical and reduces it to DPPH-H form and consequently, the absorbance decreases. The degree of discoloration reveals the antioxidant compound's scavenging capacity as well as its hydrogen-donating ability [51]. As seen in Figure 14, the title compound exhibited a moderate free radical scavenging activity compared with BHT thus, a concentration of 4000 µg/mL inhibited 35.3 % compared with BHT (78 %). In general, the antioxidant activity is expressed in terms of IC_{50}, which is the concentration of the antioxidant that decreases the 50 % of DPPH [52]. However, in this study the 50 % of DPPH inhibition by $(H_2en)_2(NH_4)_2\{V_{10}O_{28}\}.4H_2O$ wasn't achieved; thus, the concentrations used in this study were not sufficient to inhibit the IC_{50} of inhibition. The ferric reducing power test FRAP was used to evaluate the title compound's reducing power.

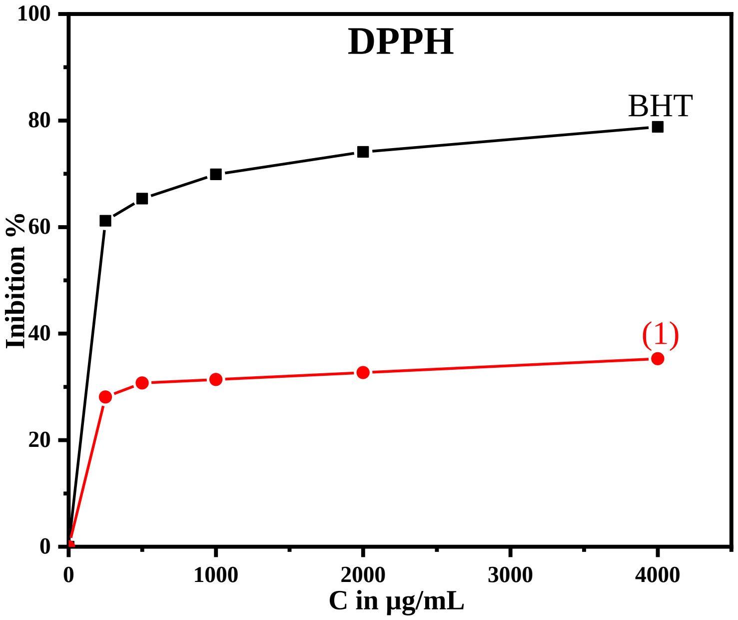

Fig. 14. Free radical scavenging activity vs. BHT of $(H_2en)_2(NH_4)_2\{V_{10}O_{28}\}.4H_2O$. with 1 = $(H_2en)_2(NH_4)_2\{V_{10}O_{28}\}.4H_2O$.

This latter measures the reducing potency of extract and standard antioxidants; thus, higher absorbance indicates higher reducing potency. The mechanism involved in this essay is based on a single-electron transfer system [53]. As depicted in Figure 15, there was a significant difference between the reducing power of $(H_2en)_2(NH_4)_2\{V_{10}O_{28}\}.4H_2O$ and the gallic acid even with high concentrations. In the majority of times, we use different methods to evaluate the antioxidant activity. Therefore, The FRAP test was chosen because it is rapid and easy to carry out, and the reaction is repeatable and linearly related to Biskup *et al.* [54].

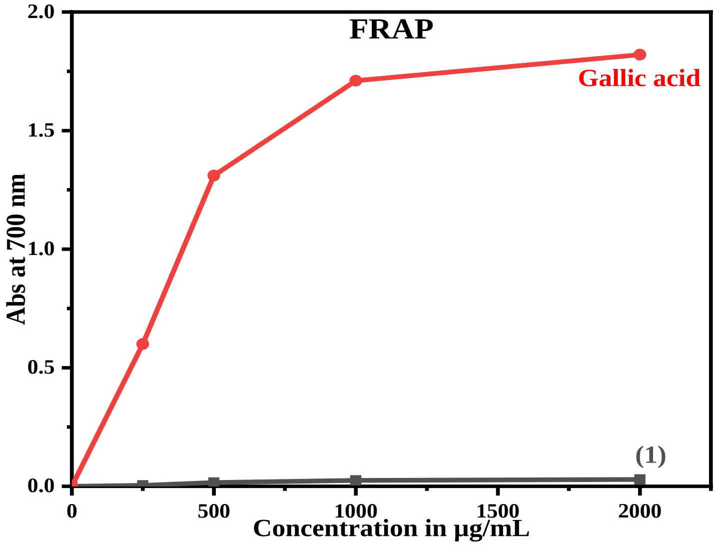

Fig. 15. Ferric reducing power vs. gallic acid of $(H_2en)_2(NH_4)_2\{V_{10}O_{28}\}.4H_2O$.
with 1 = $(H_2en)_2(NH_4)_2\{V_{10}O_{28}\}.4H_2O$.

The phosphomolybdenum test measures total antioxidant activity and provides a direct estimate of an antioxidant's reducing power. Particularly, this test is based on the reducing capacity of the Mo(VI) to Mo(V) by an antioxidant and the formation of a green complex of Mo(V) at an acidic pH and higher temperature of 95 °C. A seen in Figure 16, and comparing with gallic acid, the complex revealed a moderate antioxidant capacity similar to the previous results obtained using the DPPH test.

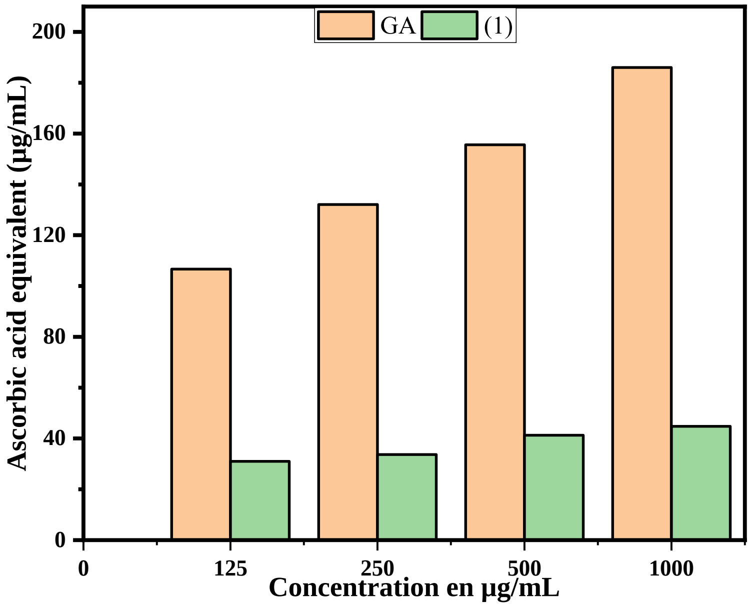

Fig. 16. Total antioxidant capacity of $(H_2en)_2(NH_4)_2\{V_{10}O_{28}\}.4H_2O$ vs. gallic acid.
with 1 = $(H_2en)_2(NH_4)_2\{V_{10}O_{28}\}.4H_2O$.

We believe that no other authors have investigated the antioxidant properties of $(H_2en)_2(NH_4)_2\{V_{10}O_{28}\}.4H_2O$. Our findings demonstrated the moderate antioxidant activity of the title compound confirmed by three validated antioxidants tests.

4. Conclusion

The hybrid ethylenediamine/$V_{10}O_{28}$ compound was elaborated applying simple instrumental equipment, affordable reactants and the use of water as a solvent, which conforms to the concept of "green chemistry". $N-H\cdots O$ and $O-H\cdots O$ hydrogen bonds connect the decavanadate anions, ethylenediammonium cations, ammonium cations, and water molecules to create a complex three-dimensional network of $(H_2en)_2\{V_{10}O_{28}\}.4H_2O$. The IR reveals the presence of the VO6 octahedron, the ethylenediammonium and ammonium cations, and the water molecule, which matches the single-crystal X-ray structural investigation results. The thermogravimetric study reveals that the decomposition of the hybrid vanadate occurs in three stages, with the loss of the organic moiety, ammonium cation, water molecules, and decavanadate degradation. Electrochemical measurements confirmed that yellow decavanadates. solutions in 3% NaCl exhibited no significant inhibition efficiency and increasing decavanadate concentration was unfavorable. Besides clear metavanadate solutions in 1 M HCl containing monovanadate exhibited strong inhibition. In addition to vanadate ions, a variety of other atoms including Nitrogen and Oxygen have also been intercalated with the surface gallery to promote the anticorrosive properties. In addition, it should be noted that the inhibiting efficiencies calculated from EIS data follow the same trend as those obtained from Tafel and LPR methods, though some differences, reflecting the approximations on which each of them is based. The biological activity of $(H_2en)_2(NH_4)_2\{V_{10}O_{28}\}.4H_2O$ shows mediocre antimicrobial and antioxidant activities.

Declaration of competing interest

The authors state that they have no known competing financial interests or personal ties that might have influenced the research presented in this paper.

Acknowledgements

We are grateful for measurement time on the X-ray diffraction platform PMD²X of the Institute Jean Barriol (University of Lorraine, France). The authors are also very indebted to the members of LIMAS laboratory for carrying out the electrochemical studies in terms of enhancing the anticorrosion properties of decavanadate.

References

[1] A.S. Tracey, G.R. Willsky, E.S. Takeuchi., "Vanadium Chemistry, biochemistry, pharmacology and practical applications", CRC Press, (2007).

[2] D.C. Crans, B.J. Peters, X. Wu, C.C. McLauchlan, Does anion-cation organization in Na+-containing X-ray crystal structures relate to solution interactions in inhomogeneous nanoscale environments: Sodium-decavanadate in solid state materials, minerals, and microemulsions, Coord. Chem. Rev. 344 (2017) 115–130.

[3] M. Aureliano, C.A. Ohlin, Decavanadate in vitro and in vivo effects: Facts and opinions, J. Inorg. Biochem. 137 (2014) 123–130.

[4] D.C. Crans, S. Roy, Introduction for the Emergent Polyoxometalates and Soft-oxometalates thematic issue, New J. Chem. 40 (2016) 882–885.

[5] M. Aureliano, C.A. Ohlin, M.O. Vieira, M.P.M. Marques, W.H. Casey, L.A.E. Batista De Carvalho, Characterization of decavanadate and decaniobate solutions by Raman spectroscopy, Dalt. Trans. 45 (2016) 7391–7399.

[6] Jagoba Martin Caballero, Hybrid Polyoxometalates : Synthesis , Crystal Structures , Thermostructural Behavior and Anchoring to Tailored Polymeric Surfaces Jagoba Martín Caballero, 2017 (2017) 1–277.

[7] M. Aureliano, D.C. Crans, Decavanadate $(V_{10} O_{28})^{6-}$ and oxovanadates: Oxometalates with many biological activities, J. Inorg. Biochem. 103 (2009) 536–546.

[8] M.W. Kendig, R.G. Buchheit, Corrosion inhibition of aluminum and aluminum alloys by soluble chromates, chromate coatings, and chromate-free coatings, Corrosion 59 (2003) 379–400.

[9] R. G. Buchheit, Corrosion Science: A Retrospective and Current Status in Honor of Robert P. Frankenthal, The Electrochemical Society Proceedings Series, Pennington, 13(2002) 430.

[10] H. Guan, R.G. Buchheit, Corrosion protection of aluminum alloy 2024-T3 by vanadate conversion coatings, Corrosion 60 (2004) 284–296.

[11] M. Trypuć, G. Łyjak, Solubility investigations in the $NH_4Cl+NaVO_3+NH_4VO_3+NaCl+H_2O$ system at 303 K, J. Chem. Eng. Data. 45 (2000) 872–875.

[12] C. J. E. Smith, M. A. H. Hewins, P. L. Lane, K. R. Baldwin, and M. C. Gibson, in *Proceedings of Eurocorr*, Utrecht, The Netherlands, (1998) 5.

[13] M. Iannuzzi, T. Young, G.S. Frankel, Aluminum Alloy Corrosion Inhibition by Vanadates, J. Electrochem. Soc. 153 (2006) B533.

[14] Rigaku Oxford Diffraction. 2018. CrysAlis CCD and CrysAlis RED. (Versions 1.171.39.46).

[15] G.M. Sheldrick, Crystal structure refinement with SHELXL, Acta Cryst. C71 (2015) 3–8. https://doi.org/10.1107/S2053229614024218.

[16] L.J. Farrugia, WinGX suite for small-molecule single-crystal crystallography,J. Appl. Cryst. 32 (1999) 837–838.

[17] K. Brandenburg, H. Putz, Crystal Impact GbR, Postfach 1251, D 53002 Bonn, (2005) Germany.

[18] M. Balouiri, M. Sadiki, S.K. Ibnsouda, Methods for in vitro evaluating antimicrobial activity: A review, J. Pharm. Anal. 6 (2016) 71–79.

[19] W. Brand-Williams, M.E. Cuvelier, C. Berset, Use of a free radical method to evaluate antioxidant activity, LWT - Food Sci. Technol. 28 (1995) 25–30.

[20] M. Oyaizu, Studies on products of browning reaction. Antioxidative activities of products of browning reaction prepared from glucosamine, Japanese J. Nutr. Diet. 44 (1986) 307–315.

[21] P. Prieto, M. Pineda, M. Aguilar, Spectrophotometric quantitation of antioxidant capacity through the formation of a phosphomolybdenum complex: Specific application to the determination of vitamin E, Anal. Biochem. 269 (1999) 337–341.

[22] J.M. Hughes, M. Schindler, J.Rakovan, F.E. Cureton, The crystal structure of hummerite, $KMg(V_5O_{14}).8H_2O$: bonding between the $[V_{10}O_{28}]^{6-}$ structural unit and the $\{K_2Mg_2(H_2O)_{16}\}^{6+}$ interstitial complex. The Canadian Mineralogist, 40(2002) 1429-1435.

[23] A.G. Swallow, F.R. Ahmed, W.H. Barnes, The crystal structure of pascoite, $Ca_3V_{10}O_{28}.16H_2O$, Acta Crystallogr. 21 (1966) 397–405.

[24] C.F. MacRae, I. Sovago, S.J. Cottrell, P.T.A. Galek, P. McCabe, E. Pidcock, M. Platings, G.P. Shields, J.S. Stevens, M. Towler, P.A. Wood, Mercury 4.0: From visualization to analysis, design and prediction, J. Appl. Crystallogr. 53 (2020) 226–235.

[25] I.D. Brown, The Bond-Valence Method: An Empirical Approach to Chemical Structure and Bonding' in *Structure and Bonding in Crystals* (M. O'Keeffe & A. Navrotsky, eds.) New York, Academic Press. II, 1–30 (1981).

[26] N. Boşnjaković-Pavlović, J. Prévost, A. Spasojević-De Biré, Crystallographic statistical study of decavanadate anion based-structures: Toward a prediction of noncovalent interactions, Cryst. Growth Des. 11 (2011) 3778–3789.

[27] K.P. Jin, H.J. Jiang, Y. Wang, D.P. Zhang, J. Mei, S.H. Cui, Synthesis and Crystal Structure of Decavanadate-Based Coordination Polymers, J. Clust. Sci. 29 (2018) 785–792.

[28] M.K. Marchewka, M. Drozd, Ethylenediammonium dication: H-bonded complexes with terephthalate, chloroacetate, phosphite, selenite and sulfamate anions. Detailed vibrational spectroscopic and theoretical studies of ethylenediammonium terephthalate, Spectrochim. Acta - Part A Mol. Biomol. Spectrosc. 99 (2012) 223–233.

[29] N.R. Putrevu, R.J. Doedens, M.I. Khan, Decavanadate with a novel coordination complex: Synthesis and characterization of $(NH_4)_2[Ni(H_2O)\ 5(NH_3)]_2(V_{10}O_{28})$ ·4H2O, Inorg. Chem.

Commun. 38 (2013) 5–7.

[30] I. Omri, T. Mhiri, M. Graia, Novel decavanadate cluster complet $(HImz)_{12}(V_{10}O_{28})_{23}H_2O$: Synthesis, characterization, crystal structure, optical and thermal properties, J. Mol. Struct. 1098 (2015) 324–331.

[31] S. Chalotra, R.A. Mir, G. Kaur, O.P. Pandey, Oxygen deficient V2O3: A stable and efficient electrocatalyst for HER and high performance EDLCs, Ceram. Int. 46 (2020) 703–714.

[32] K.D. Ralston, T.L. Young, R.G. Buchheit, Electrochemical Evaluation of Constituent Intermetallics in Aluminum Alloy 2024-T3 Exposed to Aqueous Vanadate Inhibitors, J. Electrochem. Soc. 156 (2009) C135.

[33] K.D. Ralston, S. Chrisanti, T.L. Young, R.G. Buchheit, Corrosion Inhibition of Aluminum Alloy 2024-T3 by Aqueous Vanadium Species, J. Electrochem. Soc. 155 (2008) C350.

[34] M. Aureliano, Decavanadate: A journey in a search of a role, Dalt. Trans. (2009) 9093–9100.

[35] J.S. Valente, E. Maya-Flores, H. Armendáriz-Herrera, R. Quintana-Solórzano, J.M. López Nieto, Metal solution precursors: Their role during the synthesis of MoVTeNb mixed oxide catalysts, Catal. Sci. Technol. 8 (2018) 3123–3132.

[36] E. BiÇer, N. Dege, E. Coşkun, Synthesis, characterization and crystal structure of a novel decavanadate salt, $[V_{0.50}(H_2O)_5]_2[H_2(V_{10}O_{28})]\cdot4(H_2O)$, J. Chil. Chem. Soc. 62 (2017) 3610–3614.

[37] S.S. Soares, C. Gutiérrez-merino, M. Aureliano, DECAVANADATE TOXICITY EFFECTS FOLLOWING in vivo ADMINISTRATION, 661 (2015) 1–27.

[38] V.D.K. Zhetcheva, L.P. Pavlova, Synthesis and spectral characterization of a decavanadate/chitosan complex, Turkish J. Chem. 35 (2011) 215–223.

[39] C.A. Rice-Evans, N.J. Miller, G. Paganga, Structure-antioxidant activity relationships of flavonoids and phenolic acids, Free Radic. Biol. Med. 20 (1996) 933–956.

[40] J. Wang, C. N. Cao, J. J. Chen, M. Zhang,G. Ye, &H. Lin. Anodic desorption of inhibitors I. The phenomenon of anodic desorption of inhibitors. J. Chin. Soc. Corros. Prot. 15 (1995) 241–246.

[41] S. Aourabi, M. Driouch, M. Sfaira, F. Mahjoubi, B. Hammouti, C. Verma, E.E. Ebenso, L. Guo, Phenolic fraction of Ammi visnaga extract as environmentally friendly antioxidant and corrosion inhibitor for mild steel in acidic medium, J. Mol. Liq. 323 (2021) 114950. https://doi.org/10.1016/j.molliq.2020.114950.

[42] E.S. Ferreira, C. Giacomelli, F.C. Giacomelli, A. Spinelli, Evaluation of the inhibitor effect of L-ascorbic acid on the corrosion of mild steel, Mater. Chem. Phys. 83 (2004) 129–134.

[43] JO'M, Bockris, S. Srinivasan, Elucidation of the Mechanism of Electro- Lytic HYDROGEN Evolution By the Use of H-T Separation Factors *, 9 (1964) 31–44. https://doi.org/10.1016/0013-4686(64)80003-7.

[44] G.J. Brug, A.L.G. van den Eeden, M. Sluyters-Rehbach, J.H. Sluyters, The analysis of electrode impedances complicated by the presence of a constant phase element, J. Electroanal. Chem. 176 (1984) 275–295.

[45] MT-Lab/EC-Lab – Application Note #04

[46] F.B. Growcock, R.J. Jasinski, Time-Resolved Impedance Spectroscopy of Mild Steel in Concentrated Hydrochloric Acid, J. Electrochem. Soc. 136 (1989) 2310–2314.

[47] M. Lebrini, F. Bentiss, N.E. Chihib, C. Jama, J.P. Hornez, M. Lagrenée, Polyphosphate derivatives of guanidine and urea copolymer: Inhibiting corrosion effect of Armco iron in acid solution and antibacterial activity, Corros. Sci. 50 (2008) 2914–2918.

[48] M. Keddam, O.R. Mattos, H. Takenouti, Reaction Model for Iron Dissolution Studied by Electrode Impedance: II . Determination of the Reaction Model, J. Electrochem. Soc. 128 (1981) 266–274.

[49] A. Popova, M. Christov, A. Vasilev, Inhibitive properties of quaternary ammonium bromides of N-containing heterocycles on acid mild steel corrosion. Part II: EIS results, Corros. Sci. 49 (2007) 3290–3302.

[50] S. Chen, G. Wu, D. Long, Y. Liu, Preparation, characterization and antibacterial activity of chitosan-Ca3V10O28 complex membrane, Carbohydr. Polym. 64 (2006) 92–97.

[51] T.C. Shekhar, G. Anju, Antioxidant Activity by DPPH Radical Scavenging Method of Ageratum conyzoides Linn. Leaves, Am. J. Ethnomedicine. 1 (2014) 244–249.

[52] R. Scherer, H.T. Godoy, Antioxidant activity index (AAI) by the 2,2-diphenyl-1-picrylhydrazyl method, Food Chem. 112 (2009) 654–658.

[53] D. Huang, O.U. Boxin, R.L. Prior, The chemistry behind antioxidant capacity assays, J. Agric. Food Chem. 53 (2005) 1841–1856.

[54] I. Biskup, I. Golonka, Z. Sroka, A. Gamian, Antioxidant activity of selected phenols estimated by ABTS and FRAP methods. Postepy Hig Med Dosw. 67 (2013) 958–963.